J Comput Electron
DOI 10.1007/s10825-014-0579-7

Role of inelastic electron–phonon scattering in electron transport through ultra-scaled amorphous phase change material nanostructures

Jie Liu · Xu Xu · M. P. Anantram

© Springer Science+Business Media New York 2014

Abstract The electron transport through ultra-scaled amorphous phase change material (PCM) GeTe is investigated by using ab initio molecular dynamics, density functional theory, and non-equilibrium Green's function, and the inelastic electron–phonon scattering is accounted for by using the Born approximation. It is shown that, in ultra-scaled PCM device with 6 nm channel length, $<4\,\%$ of the energy carried by the incident electrons from the source is transferred to the atomic lattice before reaching the drain, indicating that the electron transport is largely elastic. Our simulation results show that the inelastic electron–phonon scattering, which plays an important role to excite trapped electrons in bulk PCM devices, exerts very limited influence on the current density value and the shape of current–voltage curve of ultra-scaled PCM devices. The analysis reveals that the Poole–Frenkel law and the Ohm's law, which are the governing physical mechanisms of the bulk PCM devices, cease to be valid in the ultra-scaled PCM devices.

Keywords Phase change material · Non-equilibrium Green's function (NEGF) · Electron phonon scattering · Mean free path (MFP) · Ultra-scaled nanostructure

1 Introduction

The phase change material (PCM) based technology is promising to become the next-generation mainstream non-volatile information storage technology [1–29]. It is known that the bulk (say, tens of nm and beyond) amorphous phase PCM exhibits a lot of interesting and useful electrical transport properties. In the sub-threshold bias region, the current–voltage curve is linear (exponential) when the bias is small (large). When the bias is larger than the threshold voltage, the current–voltage curve becomes super-exponential and the S-shape snapback occurs [6]. The inelastic electron–phonon scattering plays a crucial role to determine these measured phenomena, by exciting the trapped electrons to participate in the transport (Poole–Frenkel effect) [7–9].

Interestingly, when the PCM devices are ultra-scaled (sub-10 nm), these measured transport properties are still preserved [10]. Unfortunately, though the underlying physics of the electron transport in bulk PCM has been well studied [6–9], the ultra-scaled PCM electron transport physics is still poorly understood. Despite the lacking of thorough theoretical understanding, the state-of-art scaling experiments have shown that the PCM devices scaled down to 6.0 nm still can operate stably [10]. Also, it is known that the phase change properties can be kept in sub-2 nm PCM nanostructures [6,11–18]. The superb scalability of the PCM technology revealed in these studies has spurred intensive interests to develop ultra-scaled PCM devices, in order to enable the promising ultra-dense non-volatile information storage solutions.

In order to better understand the underlying physics and to improve the design of ultra-scaled PCM devices, it is pressing to investigate the electron transport properties in ultra-scaled PCM nanostructures. Following our previous work on the ultimate scalability [1] and the sub-threshold electron transport properties [2] of ultra-scaled PCM nanostructures, this paper focuses on the role of inelastic electron–phonon scattering in the electron transport through ultra-scaled amorphous PCM by using modeling and simulation. Here, we focus on the binary prototypical chalcogenide PCM GeTe. In Sect. 2, the modeling methodology is described. In Sect. 3,

J. Liu (✉) · X. Xu · M.P. Anantram
Department of Electrical Engineering, University of Washington, Seattle, WA 98195, USA
e-mail: liujie@uw.edu

Published online: 16 May 2014

the analysis results are shown. In Sect. 4, a brief conclusion and discussion are presented.

2 Methodology

In this section, the analysis methodology is introduced. First, the ab initio simulation procedure used to create the electron transport simulation model is described. Then, the numerical algorithms used to simulate the electron transport and to account for the inelastic electron–phonon scattering are presented.

2.1 Simulation model creation

The amorphous GeTe model is generated by using the melt-quench ab initio molecular dynamics (AIMD) simulations, which is based on the density functional theory (DFT) [1–3,19–29]. In the first step, the rhombohedral crystalline phase GeTe is melted into liquid phase at 1,100 K for 10 ps and then quenched to 300 K in 15 ps to obtain the amorphous phase. In the second step, the conjugate gradient (CG) algorithm is used to relax the amorphous phase and obtain the amorphous GeTe atomic coordinates. In the third step, the amorphous GeTe is sandwiched by two TiN electrodes and the Ge, Te, Ti, and N atoms near the TiN/GeTe interfaces are relaxed by using CG to create the electron transport simulation model as shown in Fig. 1. More details of the simulation model can be found in our previous work [1].

2.2 Non-equilibrium Green's function

After the simulation model as shown in Fig. 1 is created, the DFT simulation is performed to obtain the Hamiltonian matrix $\mathbf{H}_{\mu\nu} = \langle\phi_\mu|\hat{H}|\phi_\nu\rangle$ and the overlap matrix $\mathbf{S}_{\mu\nu} = \langle\phi_\mu|\phi_\nu\rangle$ in the pseudo-atomic orbital (PAO) representation ($\mu, \nu = 1, 2, \ldots, N_{\mathrm{PAO}}$, where N_{PAO} is the number of PAO), where $\hat{H}$ is the Hamiltonian operator of the Kohn-Sham single-particle Schrödinger equation $\hat{H}\psi_i = \epsilon_i\psi_i$; ϵ_i is the eigenvalue; $\psi_i = \sum_\mu c_{i\mu}\phi_\mu$ is the eigenstate; ϕ_μ is the PAO; $c_{i\mu}$ is the linear expansion coefficient [30].

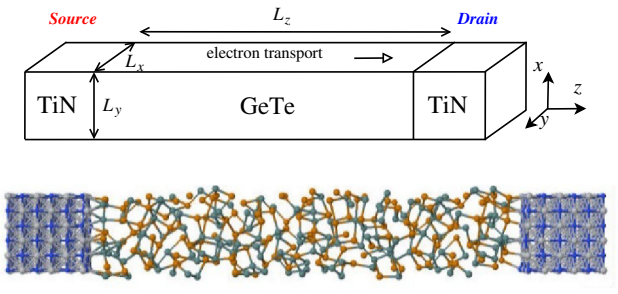


Fig. 1 Electron transport simulation model ($L_x = L_y = 1.2$ nm, $L_z = 6.0$ nm) [1]

The Hamiltonian matrix $\mathbf{H}$ and the overlap matrix $\mathbf{S}$, which contain the ab initio description of the equilibrium (bias $v = 0$) electronic structure of the simulation model, are used as inputs of the non-equilibrium Green's function (NEGF) solver to simulate the electron transport properties [31]. The retarded Green's function $\mathbf{G}^{\mathrm{r}}$, electron Green's function $\mathbf{G}^{\mathrm{n}}$, and hole Green's function $\mathbf{G}^{\mathrm{p}}$ are defined in

$$\mathbf{G}^{\mathrm{r}} = \mathbf{A}^{-1}, \mathbf{A}\mathbf{G}^{\mathrm{n}} = \mathbf{\Sigma}^{\mathrm{in}}\mathbf{G}^{\mathrm{a}}, \mathbf{A}\mathbf{G}^{\mathrm{p}} = \mathbf{\Sigma}^{\mathrm{out}}\mathbf{G}^{\mathrm{a}} \tag{1}$$

respectively, where

$$\mathbf{A} = \epsilon\mathbf{S} - \mathbf{H} - \mathbf{\Delta H} - \mathbf{\Sigma}^{\mathrm{r}}_{\mathrm{S}} - \mathbf{\Sigma}^{\mathrm{r}}_{\mathrm{D}} - \mathbf{\Sigma}^{\mathrm{r}}_{\mathrm{ph}} \tag{2}$$

The Green's functions in Eq. (1) can be solved using the recursive Green's function algorithm [32]. Here, ϵ is the electron energy; $\mathbf{\Sigma}^{\mathrm{r}}_{\mathrm{S/D}}$ is the retarded self-energy matrix due to source/drain, which are evaluated using the iterative algorithm [33]; the total in-scattering/out-scattering self-energy matrix is

$$\mathbf{\Sigma}^{\mathrm{in/out}} = \mathbf{\Sigma}^{\mathrm{in/out}}_{\mathrm{S}} + \mathbf{\Sigma}^{\mathrm{in/out}}_{\mathrm{D}} + \mathbf{\Sigma}^{\mathrm{in/out}}_{\mathrm{ph}} \tag{3}$$

the in-scattering ($\mathbf{\Sigma}^{\mathrm{in}}_{\mathrm{S/D}}$) and out-scattering ($\mathbf{\Sigma}^{\mathrm{out}}_{\mathrm{S/D}}$) self-energy matrices due to source/drain are defined as

$$\begin{aligned}\mathbf{\Sigma}^{\mathrm{in}}_{\mathrm{S/D}} &= -2\mathrm{Im}\left(\mathbf{\Sigma}^{\mathrm{r}}_{\mathrm{S/D}}\right) f_{\mathrm{S/D}},\\ \mathbf{\Sigma}^{\mathrm{out}}_{\mathrm{S/D}} &= -2\mathrm{Im}\left(\mathbf{\Sigma}^{\mathrm{r}}_{\mathrm{S/D}}\right)\left(1 - f_{\mathrm{S/D}}\right)\end{aligned} \tag{4}$$

where the Fermi function of source/drain is $f_{\mathrm{S/D}} = \left[1 + e^{(\epsilon-\mu_{\mathrm{S/D}})/k_{\mathrm{B}}T}\right]^{-1}$; the electrochemical potential of source/drain is set as $\mu_{\mathrm{S/D}} = \epsilon_{\mathrm{F}} \pm q_{\mathrm{e}}v/2$; ϵ_{F} is the Fermi level under equilibrium condition; k_{B} is the Boltzmann constant; q_{e} is the elementary charge; T is the room temperature; and v is the bias between source and drain.

Since the channel length of the ultra-scaled PCM device of our interests here is very small ($L_z = 6.0$ nm in Fig. 1), the potential varies roughly linearly from source to drain. Therefore, $\mathbf{\Delta H}_{\mu\nu} \approx \left(v_\mu + v_\nu\right)/2$ is used to in Eq. (2) account for the potential variation when bias v is applied, where v_μ is the potential at the atom to which the PAO ϕ_μ belongs.

2.3 Electron–phonon coupling

To account for the electron–phonon scattering, the retarded, in-scattering, and out-scattering electron–phonon interaction self-energy matrices $\mathbf{\Sigma}^{\mathrm{r}}_{\mathrm{ph}}$, $\mathbf{\Sigma}^{\mathrm{in}}_{\mathrm{ph}}$, and $\mathbf{\Sigma}^{\mathrm{out}}_{\mathrm{ph}}$ are included in the NEGF formalism as shown in Eq. (1–3) [31]. The imaginary part of $\mathbf{\Sigma}^{\mathrm{r}}_{\mathrm{ph}}$ is evaluated using

$$\mathrm{Im}\left(\mathbf{\Sigma}^{\mathrm{r}}_{\mathrm{ph}}\right) = -\frac{1}{2}\mathrm{Re}\left(\mathbf{\Sigma}^{\mathrm{in}}_{\mathrm{ph}} + \mathbf{\Sigma}^{\mathrm{out}}_{\mathrm{ph}}\right) \tag{5}$$

The real part of $\mathbf{\Sigma}^{\mathrm{r}}_{\mathrm{ph}}$ is ignored to alleviate the computational burden, since the influence of the real part is small [34].

Following the Born approximation, the $\mathbf{\Sigma}^{\text{in}}_{\text{ph}}$ and $\mathbf{\Sigma}^{\text{out}}_{\text{ph}}$ are calculated using

$$\begin{aligned}\mathbf{\Sigma}^{\text{in}}_{\text{ph},\mu\nu} &= D_0 \left\{ n_{\text{B}}\left(\hbar\omega\right) \mathbf{G}^{\text{n}}_{\mu\nu}\left(\epsilon - \hbar\omega\right) \right. \\ &\quad \left. + \left[n_{\text{B}}\left(\hbar\omega\right) + 1 \right] \mathbf{G}^{\text{n}}_{\mu\nu}\left(\epsilon + \hbar\omega\right) \right\} \qquad (6) \\ \mathbf{\Sigma}^{\text{out}}_{\text{ph},\mu\nu} &= D_0 \left\{ \left[n_{\text{B}}\left(\hbar\omega\right) + 1 \right] \mathbf{G}^{\text{p}}_{\mu\nu}\left(\epsilon - \hbar\omega\right) \right. \\ &\quad \left. + n_{\text{B}}\left(\hbar\omega\right) \mathbf{G}^{\text{p}}_{\mu\nu}\left(\epsilon + \hbar\omega\right) \right\} \qquad (7)\end{aligned}$$

respectively. Here, n_{B} is the Boltzmann distribution; $\hbar\omega$ is the phonon energy; and D_0 is the electron–phonon coupling strength.

Physically, Eq. (6–7) treat phonons as an infinite reservoir. The scattering of electrons by phonons is characterized by two parameters $\hbar\omega$ and D_0, which define the phonon energy and the electron–phonon coupling strengths, respectively. For simplicity, we use a single phonon mode with an energy of $\hbar\omega = 20$ meV. Experiments report that crystalline GeTe has a dominant coherent phonon at this energy [35] but the investigation of the phonon spectrum deserves further attention in both amorphous and crystalline GeTe. While measured D_0 value of the PCM is unknown, it is to be phenomenologically estimated in the following analysis, by using the measured mean free path (MFP) value.

2.4 Mean free path

Since the electron–phonon coupling strength D_0 in Eq. (6–7) controls the intensity of the electron–phonon scattering, the MFP of electrons is influenced by D_0. Though the measured value of D_0 is not available, the electron MFP has been experimentally measured, fortunately. So, in the analysis, D_0 is phenomenologically chosen, such that the consequent MFP can match the measured value. In the analysis, the MFP is calculated using

$$\begin{aligned}\text{MFP} &= \sum_{\epsilon_i > E_{\text{c}}} v\left(\epsilon_i\right) \tau\left(\epsilon_i\right) w_{\text{MFP}}\left(\epsilon_i\right), \\ w_{\text{MFP}}\left(\epsilon_i\right) &= \frac{f\left(\epsilon_i\right) \text{DOS}\left(\epsilon_i\right)}{\sum_{\epsilon_i > E_{\text{c}}} f\left(\epsilon_i\right) \text{DOS}\left(\epsilon_i\right)} \qquad (8)\end{aligned}$$

where E_{c} is the bottom of the conduction band. The velocity of electrons in amorphous materials is not so well defined and here for simplicity, we assume that the velocity is $v\left(\epsilon_i\right) = \left[2\left(\epsilon_i - E_{\text{c}}\right)/m^*\right]$. m^* is taken to be the experimentally measured effective mass in crystalline GeTe which is equal to $0.8m_0$, where m_0 is the vacuum mass of electron [36]; τ is the electron lifetime, which is defined as

$$\begin{aligned}\tau^{-1}\left(\epsilon_i\right) &= \sum_{\mu} \frac{-2}{\hbar} \text{Im}\left[\mathbf{\Sigma}^{\text{r}}_{\text{ph}}\left(\epsilon_i\right)\right] w_{\tau^{-1}}\left(\epsilon_i\right), \\ w_{\tau^{-1}}\left(\epsilon_i\right) &= \frac{\left|c_{i\mu}\right|^2}{\sum_{\mu}\left|c_{i\mu}\right|^2} \qquad (9)\end{aligned}$$

and f and DOS are the Fermi function and density of states, respectively. Here, the weighting coefficient w_{MFP} ($w_{\tau^{-1}}$) means that the eigenstate (PAO) with larger electron population exert larger impact on the MFP (τ^{-1}) [37].

2.5 Numerical implementation

The AIMD, CG, and DFT algorithms used in this paper are implemented in the SIESTA package [30]. The Γ-point is used to sample the Brillouin Zone; the plane wave cutoff is chosen to be 100 Ry; the generalized gradient approximation (GGA) of Perdew, Burke, and Ernzerhof (PBE) is used to approximate the exchange-correlation energy; the double-zeta (single-zeta) PAO is used for Ge and Te (Ti and N) atoms; and the CG relaxation convergence criteria is set as 40 meV/Å.

The NEGF simulations are parallelized over electron energies. To reduce the computational cost, the Hamiltonian matrix $\mathbf{H}$ and overlap matrix $\mathbf{S}$ are partitioned into multiple principal layers, by taking advantage of the localized nature of PAO and the consequent tri-diagonal nature of $\mathbf{H}$ and $\mathbf{S}$. The NEGF simulation with inelastic electron–phonon scattering consists of two steps: (a) the Green's functions are calculated from the electron–phonon self-energies by solving Eq. (1–3); (b) the electron–phonon self-energies are calculated from the Green's functions by solving Eq. (5–7). These two steps iterate until the convergence criteria [37]

$$\left| \left(n^{(i)}_{\text{A}} - n^{(i-1)}_{\text{A}} \right) / n^{(i-1)}_{\text{A}} \right| < \eta \qquad (10)$$

$$\left| \left(p^{(i)}_{\text{A}} - p^{(i-1)}_{\text{A}} \right) / p^{(i-1)}_{\text{A}} \right| < \eta \qquad (11)$$

are reached. η is chosen to be 0.01. $n^{(i)}_{\text{A}}$ and $p^{(i)}_{\text{A}}$ are the electron and hole densities at atom A, in the i^{th} iteration of the self-consistent Born loop and are given by

$$n_{\text{A}} = \frac{1}{2\pi} \sum_{\mu \in \text{A}} \sum_{\nu} \int_{-\infty}^{+\infty} d\epsilon \mathbf{G}^{n}_{\mu\nu}\left(\varepsilon\right) \mathbf{S}_{\mu\nu} \qquad (12)$$

$$p_{\text{A}} = \frac{1}{2\pi} \sum_{\mu \in \text{A}} \sum_{\nu} \int_{-\infty}^{+\infty} d\epsilon \mathbf{G}^{p}_{\mu\nu}\left(\varepsilon\right) \mathbf{S}_{\mu\nu} \qquad (13)$$

3 Results

In this section, the electron transport simulation results are presented. First, the electron–phonon coupling strength is phenomenologically estimated by comparing the simulated MFP against measured value. Then, the impact of inelastic electron–phonon scattering is analyzed.

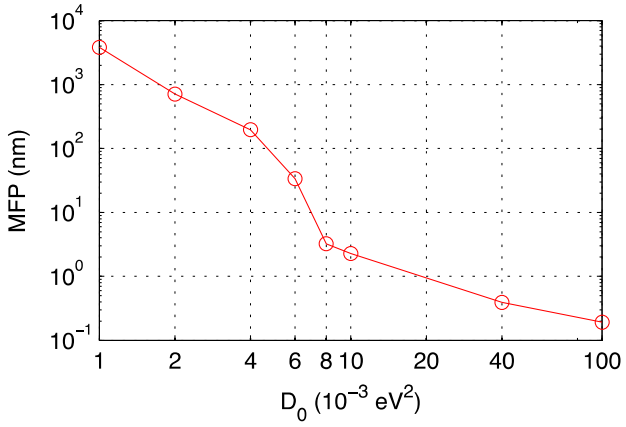


Fig. 2 Impact of electron–phonon coupling strength (D_0) on mean free path (MFP)

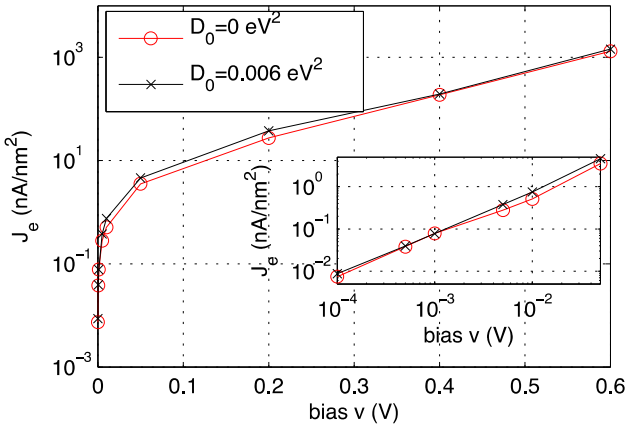


Fig. 3 Impact of inelastic electron–phonon scattering on the current–voltage curve

3.1 Electron–phonon coupling strength

As discussed in Sect. 2.4, the electron MFP is influenced by the phenomenological parameter D_0, whose value for PCM is unknown. Typically, the value of D_0 is around 10^{-2} eV^2 [34]. Here, D_0 is tuned around the neighborhood of this value, as shown in Fig. 2. It can be seen that when D_0 is increased from $10{-}3$ eV^2 to 10^{-1} eV^2, the electron MFP is decreased monotonously from about 3μm to about 2 Å. Physically, larger D_0 represents stronger electron–phonon coupling, leading to more intensive electron scattering by phonons and thus shorter electron MFP.

Experimental studies have shown that the electron MFP in PCM is at the order of 10^1 nm (e.g., larger than 10 nm for $Ge_2Sb_2Te_5$ [6], about 20 nm for GeTe and about 50 nm for Sb_2Te_5 [38], etc.). Figure 2 shows that when $D_0 = 0.006$ eV^2, the simulated electron MFP (about 30 nm) is close to the experimentally measured MFP value. This implies that $D_0 = 0.006$ eV^2 can phenomenologically represent the strength of electron–phonon coupling, in terms of the electron MFP. Therefore, in the following analysis, $D_0 = 0.006$ eV^2 is chosen as the electron–phonon coupling strength value.

3.2 Current–voltage curve

When a bias v is applied between the source and drain, the current density J_e flowing from the kth principal layer to the (k+1)th principal layer can be calculated using

$$J_e = \frac{2q_e}{\hbar L_x L_y} \int_{-\infty}^{+\infty} d\epsilon j\,(\epsilon; k)\,,$$

$$j\,(\epsilon; k) = \frac{1}{2\pi} \mathrm{Tr}\left[\mathbf{T}_{k,k+1}\mathbf{G}^{\mathrm{n}}_{k+1,k} - \mathbf{G}^{\mathrm{n}}_{k,k+1}\mathbf{T}_{k+1,k}\right] \qquad (14)$$

where $\mathbf{T}_{\mu\nu} = \epsilon\mathbf{S}_{\mu\nu} - \mathbf{H}_{\mu\nu}$; and $k = 1, 2, \ldots, N_{\mathrm{PL}}$ ($N_{\mathrm{PL}} = 8$ is the number of principal layers). Figure 3 shows the subthreshold current–voltage curves of the ultra-scaled amorphous GeTe (Fig. 1) with ($D_0 = 0.006$ eV^2) and without ($D_0 = 0$ eV^2) inelastic electron–phonon scattering. It can be seen that the measured linear (exponential) shape of the current–voltage curve when the bias is small (larger) is reproduced in our simulation. As analyzed in our previous study, the underlying physical reasons of this phenomenon can be attributed to the bias-induced change of transmission and the bias-window enlarging.

It can be seen from Fig. 3 that the inelastic electron–phonon scattering exerts very limited influence on the quantitative current density value and the qualitative current–voltage curve shape. This indicates that the electron transport in the ultra-scaled PCM devices is largely elastic. In the elastic limit ($D_0 = 0$ eV^2), the electron energy ϵ is kept the same when it is transported from source to drain. Physically, this means that the channel length of the ultra-scaled PCM devices (6 nm as shown in Fig. 1) is much smaller than the electron MFP (about tens of nm), leaving electrons little chance to be scattered before reaching the drain or to lose their energy to the lattice.

3.3 Current density distribution

The elastic nature of the electron transport in ultra-scaled PCM devices can be seen more clearly in the Fig. 4, which demonstrate the energy-resolved and position-dependent current density ($j\,(\epsilon; k)$ in Eq. (10)). Since the model is partitioned into $N_{\mathrm{PL}} = 8$ principal layers along the z-direction, there are $N_{\mathrm{PL}} - 1$ curves in each plot. Each curve represents the energy distribution of the current density at a particular cross-section along the transport direction.

It can be seen from Fig. 4 that there is a bandgap, indicating the measured semiconducting nature of amorphous

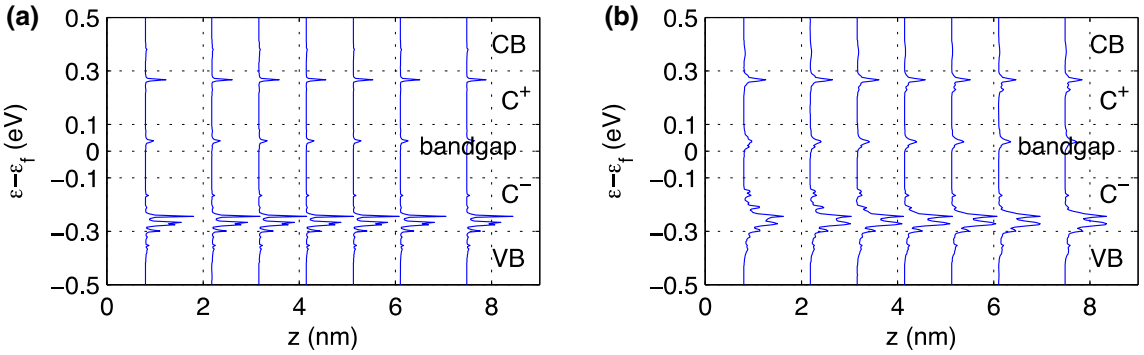


Fig. 4 Current density as a function of position z (Fig. 1) and electron energy ϵ, when the bias is 0.6 V. **a** $D_0 = 0$ eV^2; and **b** $D_0 = 0.006$ eV^2. ϵ_f, Fermi level; VB, valence band; CB, conduction band; C+, donor-like states; and C-, acceptor-like states

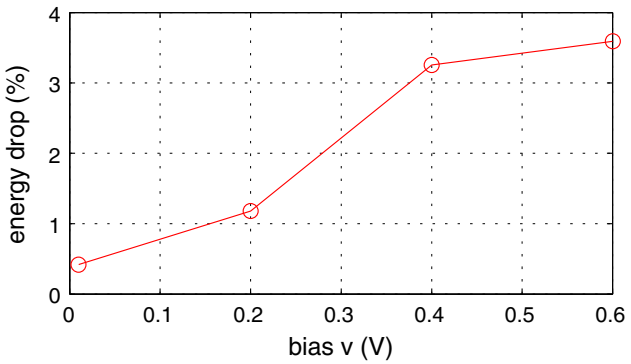


Fig. 5 Bias-dependent energy drop of electrons, i.e., $-(E_7 - E_1)/E_1$, where $E_k = \int_{-\infty}^{+\infty} \epsilon j\,(\epsilon; k)\, d\epsilon$

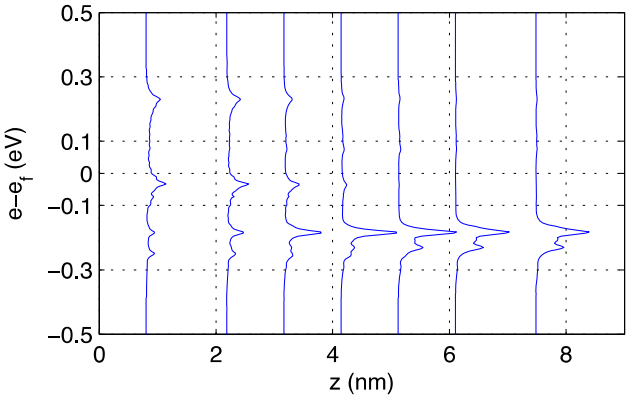


Fig. 6 The distribution of current per unit energy for various cross sections in the device when the electron–phonon scattering strength is set to an artificially high value of $D_0 = 0.01$ eV^2. A clear relaxation of carriers injected on the *left hand side* of the device is seen as the carriers transit through. The bias across the device is 0.4 V. The y-axis is energy measured from the Fermi energy and the x-axis is position from source to drain

PCM is reproduced in our simulations. It also can be seen that the electrical conduction is dominated by the electron transport via the intra-bandgap donor-like and acceptor-like states. The simulation results show that $J_p/(J_n + J_p) \approx 80\,\%$ ($J_n/(J_n + J_p) \approx 20\,\%$) of the current is due to the transport via the acceptor-like (donor-like) states, where $J_p = \int_{-\infty}^{\epsilon_F} j d\epsilon$ and $J_n = \int_{\epsilon_F}^{+\infty} j d\epsilon$. This indicates the p-type conductivity, which agrees with experimental measurements [6].

The energy locations of the peaks of the curves remain perfectly fixed in the elastic limit ($D_0 = 0$ eV^2, Fig. 4a), and largely unchanged when the inelastic electron–phonon scattering is turned on ($D_0 = 0.006$ eV^2, Fig. 4b). By comparing Fig. 4a, b, it can be seen that the inelastic electron–phonon scattering can no longer excite trapped electrons to participate in the transport, indicating the failure of the Poole–Frenkel law and the electron transport is changed from diffusive to elastic when the PCM devices are scaled from bulk to sub-10 nm. Though phonons can no longer significantly alter the energy of electrons via inelastic scattering in ultra-scaled PCM devices, they effectively broaden the peaks of the energy-resolved current density. This stems from the broadening of the defect states by the electron–phonon interaction.

3.4 Electron energy relaxation

Qualitatively, Fig. 4b shows that the electrons transport through the ultra-scaled PCM devices largely elastically, without significantly losing energy to lattice. Quantitatively, it is interesting to evaluate how much of the energy carried by the electrons is lost to lattice during the electron transport. As shown in Fig. 5, when $D_0 = 0.006$ eV^2, only a very small fraction of electron energy (<4 %) is transferred to lattice during the transport from source to drain. Interestingly, when the bias is increased, the electron energy loss slightly increases. Finally, to verify our method and ensure that the electron energy relaxes as the electron–phonon scattering strength increases, we present results of energy relaxation from source to drain for an artificially high value of the electron–phonon scattering strength, $D_0 = 0.01$ eV^2. We see from Fig. 6, that the electrons injected from the left relax in energy as they exit the right hand side of the device. The

mean free path corresponding to $D_0 = 0.01$ eV^2 is 1.7 nm (Fig. 2) while the length of the PCM region is 6 nm.

In the bulk PCM devices, the phase transitions between crystalline and amorphous phases largely rely on the thermal energy generated inside the PCM active region (Joule heating via Ohm's law), since the PCM resistivity is much larger than the electrodes. This hinges on the fact that electrons experience multiple inelastic scattering events and they exchange energy with lattice during the diffusive transport. In the ultra-scaled PCM devices, however, electrons can no longer significantly lose energy to lattice (Fig. 6) because the transport becomes elastic (Fig. 4). Therefore, the measured stable and reversible phase transitions in ultra-scaled PCM devices should be driven by either the thermal energy generated in heater electrodes and/or other physical mechanisms like thermoelectric effects.

4 Conclusion

The impact of the inelastic electron–phonon scattering on the electron transport through the ultra-scaled amorphous GeTe is investigated. It is shown that the inelastic electron–phonon scattering broadens the current density peaks but it has little influence on the quantitative current density value and qualitative shape of the current–voltage curve. The simulations show that less than 4% of the electron energy is transferred to lattice via inelastic electron–phonon scattering during the transport from source to drain in ultra-scaled PCM device whose channel length is 6 nm. The results reveal that the electron transport process is largely elastic, indicating that the Poole–Frenkel law and the Ohm's law cease to be valid in ultra-scaled PCM devices.

Acknowledgments This work was supported by U.S. National Science Foundation (NSF) under Grant Award 1006182. We acknowledge the Pacific Northwest National Laboratory (PNNL) for providing computational resources on the PNNL Chinook supercomputers. This work used the Extreme Science and Engineering Discovery Environment (XSEDE), which is supported by National Science Foundation Grant number OCI-1053575. This work was facilitated through the use of advanced computational, storage, and networking infrastructure provided by the Hyak supercomputer system, supported in part by the University of Washington's eScience Institute. We acknowledge J. Akola and R.O. Jones (for discussion about AIMD simulations).

References

1. Liu, J., Anantram, M.P.: Low-bias electron transport properties of germanium telluride ultrathin films. J. Appl. Phys. **113**(1–6), 063711 (2013)
2. Liu, J., Xu, X., Anantram, M.P.: Sub-threshold electron transport properties of ultra-scaled phase change memory. IEEE Electron Device Lett. **35**(5), 533–535 (2014). doi:10.1109/LED.2014.2311461
3. Liu, J., Xu, X., Brush, L., Anantram, M.P.: A multi-scale analysis of the crystallization of amorphous germanium telluride using ab-initio simulations and classical crystallization theory. J. Appl. Phys. **115**(1–7), 023513 (2014)
4. Liu, J., Yu, B., Anantram, M.P.: Scaling analysis of nanowire phase-change memory. IEEE Electron Device Lett. **32**, 1340–1342 (2011)
5. Liu, J., Yu, B., Anantram, M.P.: Isotropic and anisotropic scaling analysis of nanowire phase change memory. 11th IEEE Conference on Nanotechnology, pp. 1343–1347 (2011)
6. Raoux, S., Wuttig, M. (eds.): Phase Change Materials Science and Applications. Springer, New York (2009)
7. Ielmini, D.: Threshold switching mechanism by high-field energy gain in the hopping transport of chalcogenide glasses. Phys. Rev. B **78**(1–8), 035308 (2008)
8. Ielmini, D., Zhang, Y.G.: Analytical model for subthreshold conduction and threshold switching in chalcogenide-based memory devices. J. Appl. Phys. **102**(1–13), 054517 (2007)
9. Ielmini, D., Zhang, Y.G.: Evidence for trap-limited transport in the subthreshold conduction regime of chalcogenide glasses. Appl. Phys. Lett. **90**(1–3), 192102 (2007)
10. Kim, S.B., Bae, B.J., Zhang, Y., Jeyasingh, R.G.D., Kim, Y., Baek, I.G., Park, S., Nam, S.W., Wong, H.-S.P.: One-dimensional thickness scaling study of phase change material(Ge2Sb2Te5) using a pseudo 3-terminal device. IEEE Trans. Electron Device **58**, 1483–1489 (2011)
11. Simpson, R.E., Krbal, M., Fons, P., Kolobov, A.V., Tominaga, J., Uruga, T., Tanida, H.: Toward the ultimate limit of phase change in Ge2Sb2Te5. Nano Lett. **10**, 414–419 (2010)
12. Caldwell, M.A., Raoux, S., Wang, R.Y., Wong, H.-S.P., Milliron, D.J.: Synthesis and size-dependent crystallization of colloidal germanium telluride nanoparticles. J. Mater. Chem. **20**, 1285–1291 (2010)
13. Raoux, S., Jordan-Sweet, J.L., Kellock, A.J.: Crystallization properties of ultrathin phase change films. J. Appl. Phys. **103**(1–7), 114310 (2008)
14. Raoux, S., Rettner, C.T., Jordan-Sweet, J.L., Deline, V.R., Philipp, J.B., Lung, H.L.: Scaling properties of phase change nanostructures and thin films. Proc. Euro. Symp. on Phase Change and Ovonic Science, pp. 127–134 (2006)
15. Wong, H.-S.P., Kim, S., Lee, B., Caldwell, M.A., Liang, J.L., Wu, Y., Jeyasingh, R.G.D., Yu, S.M.: Recent progress of phase change memory (PCM) and resistive switching random access memory (RRAM). 10th IEEE International Conference on Solid-State and Integrated Circuit Technology, pp. 1055–1060 (2010)
16. Wong, H.-S.P., Raoux, S., Kim, S., Liang, J.L., Reifenberg, J.P., Rajendran, B., Asheghi, M., Goodson, K.E.: Phase change memory. Proc. IEEE **98**, 2201–2227 (2010)
17. Burr, G.W., Breitwisch, M.J., Franceschini, M., Garetto, D., Gopalakrishnan, K., Jackson, B., Kurdi, B., Lam, C., Lastras, L.A., Padilla, A., Rajendran, B., Raoux, S., Shenoy, R.S.: Phase change memory technology. J. Vac. Sci. Technol. B **28**, 223–262 (2010)
18. Raoux, S., Burr, G.W., Breitwisch, M.J., Rettner, C.T., Chen, Y.C., Shelby, R.M., Salinga, M., Krebs, D., Chen, S.H., Lung, H.L., Lam, C.H.: Phase-change random access memory: a scalable technology. IBM J. Res. Device **52**, 465–479 (2008)
19. Lee, T.H., Elliott, S.R.: Structural role of vacancies in the phase transition of Ge2Sb2Te5 memory materials. Phys. Rev. B **84**(1–5), 094124 (2011)
20. Lee, T.H., Elliott, S.R.: Ab initio computer simulation of the early stages of crystallization: application to Ge2Sb2Te5 phase-change materials. Phys. Rev. Lett. **107**(1–5), 145702 (2011)
21. Hegedus, J., Elliott, S.R.: Microscopic origin of the fast crystallization ability of Ge–Sb–Te phase-change memory materials. Nat. Mater. **7**, 399–405 (2008)
22. Krbal, M., Kolobov, A.V., Fons, P., Tominaga, J., Elliott, S.R., Hegedus, J., Uruga, T.: Intrinsic complexity of the melt-quenched

amorphous Ge2Sb2Te5 memory alloy. Phys. Rev. B **83**(1–8), 054203 (2011)
23. Akola, J., Jones, R.O.: Structural phase transitions on the nanoscale: The crucial pattern in the phase-change materials Ge2Sb2Te5 and GeTe. Phys. Rev. B **76**(1–10), 235201 (2007)
24. Akola, J., Jones, R.O.: Density functional study of amorphous, liquid and crystalline Ge2Sb2Te5: homopolar bonds and/or AB alternation. J. Phys. Condens. Matter **20**(1–10), 465103 (2008)
25. Akola, J., Jones, R.O.: Binary alloys of Ge and Te: order, voids, and the eutectic composition. Phys. Rev. Lett. **100**(1–4), 205502 (2008)
26. Akola, J., Jones, R.O., Kohara, S., Kimura, S., Kobayashi, K., Takata, M., Matsunaga, T., Kojima, R., Yamada, N.: Experimentally constrained density-functional calculations of the amorphous structure of the prototypical phase-change material Ge2 Sb2 Te5. Phys. Rev. B **80**(1–4), 020201 (2009)
27. Akola, J., Jones, R.O.: Structure of amorphous Ge8Sb2Te11: GeTe-Sb2Te3 alloys and optical storage. Phys. Rev. B **79**(1–8), 134118 (2009)
28. Akola, J., Larrucea, J., Jones, R.O.: Polymorphism in phase-change materials: melt-quenched and as-deposited amorphous structures in Ge2Sb2Te5 from density functional calculations. Phys. Rev. B **83**(1–7), 094113 (2011)
29. Kalikka, J., Akola, J., Larrucea, J., Jones, R.O.: Nucleus-driven crystallization of amorphous Ge2Sb2Te5: a density functional study. Phys. Rev. B **86**(1–10), 144113 (2012)
30. Soler, J.M., Artacho, E., Gale, J.D., Garca, A., Junquera, J., Ordejon, P., Sanchez-Portal, D.: The SIESTA method for ab initio order-N materials simulation. J. Phys. Condens. Matter **14**, 2745–2779 (2002)
31. Anantram, M.P., Lundstrom, M.S., Nikonov, D.E.: Modeling of nanoscale devices. Proc. IEEE **96**, 1511–1550 (2008)
32. Svizhenko, A., Anantram, M.P., Govindan, T.R., Biegel, B., Venugopal, R.: Two-dimensional quantum mechanical modeling of nanotransistors. J. Appl. Phys. **91**, 2343–2354 (2002)
33. Lopez Sancho, M.P., Lopez Sancho, J.M., Rubio, J.: Highly convergent schemes for the calculation of bulk and surface Green functions. J. Phys. F Metal Phys. **15**, 851 (1985)
34. Koswatta, S.O., Hasan, S., Lundstrom, M.S., Anantram, M.P., Nikonov, D.E.: Nonequilibrium green's function treatment of phonon scattering in carbon-nanotube transistors. IEEE Trans. Electron Devices **54**, 2339–2351 (2007)
35. Forst, M., Dekorsy, T., Trappe, C., Laurenzis, M., Kurz, H., Bechevet, B.: Phase change in Ge2Sb2Te5 films investigated by coherent phonon spectroscopy. Appl. Phys. Lett. **77**, 1964–1966 (2000)
36. Bahl, S.K.: Amorphous versus crystalline GeTe films III electrical properties and band structure. Appl. Phys. **41**, 2196–2212 (1970)
37. Liu, J.: Multiscale simulation of phase change memory. PhD thesis, University of Washington, Seattle, WA, USA
38. Yu, D., Brittman, S., Lee, J.S., Falk, A.L., Park, H.: Minimum voltage for threshold switching in nanoscale phase-change memory. Nano Lett. **8**, 3429–3433 (2008)